ORNL/NRC/LTR-99/28

Contract Program or Program Project Title:	Heavy-Section Steel Technology (HSST) Engineering Technology Division
Subject of this Document:	An Investigation of Shallow-Flaw Effects on the Master Curve Indexing Parameter (T_o) in RPV Material
Type of Document:	Letter Report
Authors:	W. J. McAfee P. T. Williams B. R. Bass D. E. McCabe
Date Published:	April 2000
Responsible NRC Individual and NRC Office or Division	M. T. Kirk Division of Engineering Technology Office of Nuclear Regulatory Research U. S. Nuclear Regulatory Commission

Prepared for the
U.S. Nuclear Regulatory Commission
Washington, D.C. 20555-0001
Under Interagency Agreement DOE 1886-N011-9B
NRC JCN No. B0119

OAK RIDGE NATIONAL LABORATORY
Oak Ridge, Tennessee 37831-8056
managed and operated by
UT-Battelle, LLC
for the
U. S. DEPARTMENT OF ENERGY
under Contract No. DE-AC05-00OR22725

ORNL/NRC/LTR-99/28

An Investigation of Shallow-Flaw Effects on the Master Curve Indexing Parameter (T_o) in RPV Material

W. J. McAfee, P. T. Williams, B. R. Bass, and D. E. McCabe
Oak Ridge National Laboratory
Oak Ridge, TN

Manuscript Completed—February 2000
Date Published—April 2000

Prepared for the
U.S. Nuclear Regulatory Commission
Office of Nuclear Regulatory Research
Under Interagency Agreement DOE 1886-N011-9B

NRC JCN No. B0119

Prepared by the
OAK RIDGE NATIONAL LABORATORY
Oak Ridge, Tennessee 37831-8056
managed and operated by
UT-Battelle, LLC
for the
U. S. DEPARTMENT OF ENERGY
under Contract No. DE-AC05-00OR22725

An Investigation of Shallow-Flaw Effects on the Master Curve Indexing Parameter (T_o) in RPV Material

W. J. McAfee, P. T. Williams, B. R. Bass, and D. E. McCabe

Oak Ridge National Laboratory

P. O. Box 2009

Oak Ridge, TN, 37831-8056

Abstract: A testing program was defined and executed to investigate variations in the reference indexing parameter T_o determined from shallow-flaw and deep-flaw fracture-toughness data. The test data were generated from a highly-characterized A533B plate material that had been heat treated to achieve tensile properties similar to a highly irradiated RPV material. A matrix of tests using shallow-flaw (a/W = 0.10) and deep-flaw (a/W = 0.50) 1T SE(B) specimens was conducted at temperatures in the lower transition-temperature region. Constraint loss in the shallow-flaw specimens resulted in a -26.8 °C shift in transition temperature relative to the deep-flaw constraint condition when T_0 was calculated using ASTM E1921-97 procedures. The shallow-flaw data, scaled to a deep-flaw constraint condition using a Weibull stress model provided, a T_0 value comparable to that of the deep-flaw data set. When both the shallow- and deep-flaw data were constraint-adjusted to small-scale yielding (SSY), the shifts in T_0 were -35.5 °C and -8.1 °C, respectively.

1. Introduction

A primary focus of the Heavy-Section Steel Technology (HSST) Program for the preceding ten years has been to develop an integrity assessment technology that describes shallow-flaw fracture-toughness in reactor pressure vessel (RPV) steels. This focus has been within the program's overall goal of understanding and modeling the fracture behavior or RPV steels under prototypical conditions. The factors that can significantly influence the fracture behavior include (1) flaw geometry and location, (2) multiaxial loadings, and (3) presence of cladding, (4) temperature, and (5) residual stresses. One of the principal elements affecting constraint in an RPV is flaw depth. From prior studies of the comparative behavior of shallow and deep flaws in single-edge notched bend [SE(B)] specimens, it has been shown that the mean value and scatter of shallow-flaw fracture toughness obtained from RPV material are higher than those for deep-flaw data [1-3]. The difference in behavior is attributed to relaxation of crack-tip constraint in shallow surface flaws as the plastic zone around the flaw tip interacts with the near-free surface. Pennell, et al. [4], and Dickson, et al. [5], discussed the impact of shallow-flaw toughness on RPV integrity assessments. Whereas their findings must be considered preliminary, the potential exists for a reduction in the probability of failure as compared to evaluations using conventional deep-flaw

toughness values. Implications of the latter for RPV integrity assessment provide encouragement for full development of a shallow-flaw fracture technology.

An important element in implementing a shallow-flaw technology is the definition of the appropriate temperature indexing parameter for fracture-toughness data. The conventional indexing parameter has been RT_{NDT}, but in recent years a new parameter, T_o, has been developed and is receiving much attention. The methodology for determining T_o for two-dimensional flaws under sufficiently controlled conditions has recently been published in ASTM Standard E1921-97 [6]. A technical basis document for this "Master Curve" methodology has also been prepared and issued [7]. For ferritic steels in the ductile-to-brittle fracture-mode transition regime, the indexing parameter is determined by performing toughness tests on specimens with deep flaws (crack-depth-to-specimen-width ratio, $a/W \approx 0.5$). These tests are then used to establish a material-specific transition-temperature-range indexing parameter, T_o. Following the ASTM lead, the ASME has recently issued Code Case N-629 for implementing the Master Curve methodology into RPV integrity assessments [8]. In typical RPVs, however, the flaws having the highest probability of occurrence are shallow flaws. From the HSST cruciform-specimen testing program, there is evidence that different values of T_o may be obtained from shallow flaws subjected to different flaw-tip constraint conditions, i.e., uniaxial loading versus biaxial loading [9]. Increasing constraint causes a reduction in the shallow-flaw fracture toughness, which translates to an upward temperature shift in the toughness curve [10]. A model has been developed based on Weibull stress as a fracture parameter that predicts changes in toughness with changes in flaw-tip constraint [11]. However, this model does not directly predict a quantitative impact on the value of T_o with changes in constraint. Ruggerieri et al.[12] have addressed the problem of constraint effects on T_o through computational analysis. By adjusting small-specimen large-scale-yielding (LSY) fracture-toughness values to SSY conditions, they demonstrated the relationship between constraint loss and ΔT_o for different material strengths for Charpy size specimens. For ferritic materials, however, the SSY condition has higher constraint than that of conventional 1T specimens tested at or near T_o. To evaluate shallow-flaw effects on T_o, comparisons are more appropriately made by determining ΔT_o between 1T size shallow- and deep-flaw specimens. This was the approach taken in the present study. Specifically, reference temperature differences were compared for values obtained from experimental data using both shallow- and deep-flaw specimens (of the same material) tested at the same temperature. The experimental program was defined to measure reference temperatures for two flaw-constraint conditions.

This report describes the test program, specimen fabrication, test procedures, analyses, and interpretation of results. The results are preliminary in that they represent only one shallow-flaw

constraint condition and one material. They do provide guidance on evaluation of the effect of shallow-flaw loss-of-constraint on the indexing parameter T_o.[1]

2. Experimental Program

2.1 Test Specimen

The heat-treated HSST Plate 14A material was used as the source for this investigation, so that full advantage could be taken of an existing characterization database. Corner drop-offs remaining after machining of large-scale cruciform beams [9] provided the source blocks for the specimens. This strategy ensured that the test specimens were taken from the same general location within the plate as the cruciform beams, although prior data showed little spatial variability in properties of the heat-treated Plate 14A.

A standard ASTM 1T single-edge notch bend [SE(B)] specimen was selected for the testing program; the 1T size obviated the need for size-adjusting the test data to meet requirements of ASTM E1921 [6]. The shallow-flaw specimens were specified to contain a flaw with an *a/W* ratio of 0.10 which, in a 1T-size specimen, is difficult to fatigue precrack in conformance with ASTM E1921 requirements. Consequently, the shallow-flaw specimens were fabricated initially to have an increased width (64-mm) and a deeper flaw ($a/W \leq 0.3$), as shown in Fig. 1. The deeper flaw increased constraint and permitted fatigue precracking at lower stress levels, which in turn permitted greater control over the sharpened flaw geometry.

After fatigue precracking, the final crack-depth ratio of $a/W = 0.10$ was achieved by machining 12.7 mm (0.50-in.) from the top surface of the specimen. The standard ASTM deep-flaw specimens with $a/W = 0.5$ required no special machining. Twenty-one shallow- and nine deep-flaw SE(B) specimens were machined from the drop-off blocks. Typical shallow-flaw (before final machining) and deep-flaw specimens are shown in Fig. 2.

2.2 Test Procedures

Standard ASTM procedures were followed in testing the SE(B) specimens. A three-point bend test fixture was mounted in an environmental chamber that contained a vaporizing liquid nitrogen (LN_2) distribution system for cooling. Each test specimen was instrumented with both a crack-mouth-opening displacement (CMOD) clip gage and a load-line displacement gage. After

[1] It is recognized that the shallow-flaw SE(B) specimens discussed in this study do not meet the flaw-depth (*a/W*) geometry requirements of ASTM E-1921 and, therefore, the indexing parameter for these low-constraint specimens should be designated T_Q rather than T_0. In the interest of avoiding potential confusion associated with mixing the T_0/T_Q nomenclature, the T_0 symbol is used for both specimens in this report.

being cooled to the test temperature, the specimens were tested to failure under essentially monotonic loading. Small unloading steps were used in the initial linear-elastic part of the test to establish the elastic compliance of the specimen for calculation of slow stable crack growth.

It was first necessary to explore the temperature range where the shallow-flaw effect would be present in the shallow-flaw specimens. Testing was performed to establish a temperature where reduced constraint effects would be present and K_{Jc} values would be obtained from shallow-flaw specimens with enhanced toughness. The database of 1/2T compact tension (1/2T CT) K_{Jc} values available on this material [9] was used to assist in selection of the initial test temperature. The first shallow-flaw specimen, which was tested at -65 °C, produced a fracture-toughness value and overall fracture behavior that implied a high-constraint condition. This was confirmed by testing two deep-flaw specimens at the same temperature and comparing shallow- and deep-flaw results to the median toughness curve for the 1/2T data. Consequently, a second set of four shallow-flaw specimens was tested at a higher temperature of -55 °C. Although there was marginal separation between the shallow-flaw data and the predicted deep-flaw behavior using the 1/2T CT median curve, the differences at that temperature were judged insufficient for the purposes of this study. Based on the initial shallow-flaw results at –65°C and –55°C in conjunction with the Plate 14A 1/2T CT database, a test temperature of -20 °C was selected for testing the next set of specimens. This turned out to be an satisfactory choice and all remaining shallow- and deep-flaw specimens were tested at this temperature. The shallow-flaw and deep-flaw fracture-toughness data are summarized in Tables 1 and 2, respectively.

The fracture surface of one shallow-flaw specimen of particular interest, Specimen PBS16, is shown in Fig. 3. Examination of the precracked surface revealed that a defect had "pinned" the fatigue precrack, causing development of a highly irregular fatigue crack front. Preliminary examination indicated that this defect was a cavity with an embrittled surface. The geometry of the flaw front at this location, as well as the presence of an embrittled region, support predictions for premature cleavage initiation of this specimen. The fracture-toughness value for this specimen was well below the range of data for other shallow-flaw specimens, and was even below all deep-flaw data (see Tables 1 and 2). Such a point that falls well below the general population of a data set may be an outlier. Following ASTM E1921 procedures, such a point can be evaluated to determine if it is part of the general population of the data set or if it is from a different population and can be excluded from this data set. The procedure is as follows. The median toughness for the sixteen shallow-flaw data points, including the potential outlier, is calculated. A minimum of twelve data points is required for this to be a valid assessment. The 2 percent lower bound for the data set is next determined using this median value and constants provided in ASTM E1921. If the value of

the subject data point is less than the 2 percent lower bound for the set, it may be considered as an outlier and may be excluded from further consideration. The median value for the data set is,

$$K_{Jc(med)} = 204.8 MPa\sqrt{m}.$$

The 2 percent lower bound is determined using Eq. (14) from the Ref. 6,

$$K_{Jc(0.02)} = 0.413 K_{Jc} + 11.44 MPa\sqrt{m}$$

$$K_{Jc(0.02)} = 96.02 MPa\sqrt{m}.$$

Then, $K_{Jc(PBS16)} < K_{Jc(0.02)}$.

PBS16 can then be considered as an outlier and can be excluded from the data set. Subsequent analyses were performed both with and without this point being included just for comparison purposes.

3. Analytical Procedures and Fracture-toughness Models

3.1 Finite Element Model Development, Verification, and Validation

Sharp-tip and blunt-tip finite-element models were developed for the two SE(B) specimens depicted in Fig. 2 and were used for analysis of the fracture-toughness data given in Tables 1 and 2. The finite element meshes are shown in Fig. 4. The deep-flaw specimen (Fig. 4a) has a/W = 0.5, and the shallow-flaw specimen (Fig. 4b) has a/W = 0.1. For both specimens, the span-to-width ratio (S/W) is 4 and the width-to-thickness ratio (W/B) is 2. Blunt-tip models (see Fig. 4c) were developed for the analysis of crack-tip stress and strain fields that are required as input for the Weibull stress calculations.

The shallow-flaw and deep-flaw finite-element models were built using HSST Plate 14A material properties. Both toughness and tensile properties of that material have been extensively characterized [9]. A tensile true-stress vs true-strain curve developed for the material is shown in Fig. 5. The deep-flaw bend-bar specimen meets the geometry requirements of an SE(B) specimen in the ASTM Standard E399 [13]. Thus, the linear-elastic equations in that standard are available to verify the model. A Mode I fracture toughness, K_I, can be calculated by the following equation:

$$K_I = \left(\frac{P_Q}{B\sqrt{W}}\right)\left(\frac{S}{W}\right) f\left(a/W\right) \quad . \tag{1}$$

The crack-depth geometry factor, *f(a/W)*, is given by:

$$f(x) = \frac{3\sqrt{x}\left[1.99 - x(1-x)(2.15 - 3.93x + 2.7x^2)\right]}{2(1+2x)(1-x)^{3/2}} \tag{2}$$

where, $x = a/W$.

For both specimens, S = 203.2 mm (8.0 in.), W = 50.8 mm (2.0 in.), and B = 25.4 mm (1.0 in.), and from Eq. (2), $f(0.5)$ = 2.6625 and $f(0.1)$ = 0.84696. Linear-elastic calculations were carried out with both models for a loading up to P = 71.2 kN (16 kips), where P is the total applied load on the specimen in three-point bending. For model verification, the resulting J-integral values were then converted to stress-intensity factors by the plane-strain relation

$$K_J = +\sqrt{\left(\frac{E}{(1-\nu^2)}\right) J} \tag{3}$$

where E is Young's modulus of elasticity and ν is Poisson's ratio, values of which are shown in Fig. 5. The calculated K_J results are compared to corresponding ASTM E-399 K_I values in Fig. 6 for both specimen sizes. The close agreement for these two linear-elastic conditions serves as a verification of the model geometry, meshing, constraint conditions, and load application.

Figures 7 and 8 provide validation of the model through comparisons between the measured and predicted load versus CMOD values for the deep- and shallow-flaw tests performed at -20 °C. The deformation data are well represented by the finite-element predictions. The shallow-flaw specimens exhibit a much higher stiffness that requires substantially higher loads to achieve the same CMOD as the deep-flaw specimens.

3.2 Calibration Procedures for Weibull Cleavage-Fracture Model

It has been shown that a methodology based on Weibull stress provides a framework for constraint-based toughness scaling between different crack geometries and/or loading conditions in laboratory specimens and engineering structures [11-14]. The Weibull methodology employs a multiaxial form of the *weakest link* assumption applicable to a 3-D cracked solid where the Weibull stress, σ_w, can be characterized as a fracture parameter reflecting the local damage of the material near the crack tip. The Weibull stress, σ_w, defined by the expression

$$\sigma_w = \left[\frac{1}{V_0}\int_\Omega \sigma_q^m \, d\Omega\right]^{\frac{1}{m}} \tag{4}$$

is evaluated by integration of an equivalent tensile stress, σ_q, over the process zone. In Eq. (4), V_0 is a reference volume; m is the Weibull shape parameter; and Ω denotes the volume of the near-tip fracture process zone. Typically, Ω is defined as the contiguous volume within the contour surface $\sigma_1 \geq \lambda\sigma_0$, where σ_1 is the maximum principal stress, σ_0 is the yield stress, and λ is the *cut parameter*. A value of λ = 1.85 was used herein to achieve convergence in the calibration process for the Weibull model (described below). Also, the Weibull stress was evaluated by specifying the equivalent tensile stress to be either the maximum principal stress (MPS) or the hydrostatic (HYDRO) stress. Previous HSST studies [11] have shown that a Weibull parameter defined in terms of hydrostatic stress is useful as a fracture criterion to detect variations in constraint due to multiaxial loading conditions.

The cumulative probability of failure (P_f) by transgranular cleavage can be described in terms of a statistical fracture model (with the Weibull stress as the fracture parameter) based on a three-parameter Weibull distribution [15]

$$P_f(\sigma_w) = 1 - \exp\left[-\left(\frac{\sigma_w - \sigma_{w(min)}}{\sigma_{w(u)} - \sigma_{w(min)}}\right)^m\right] \tag{5}$$

where the parameters of the distribution are the Weibull modulus (shape parameter) m , the scaling stress (scale parameter) $\sigma_{w(u)}$, and the minimum Weibull stress for cleavage fracture (location parameter) $\sigma_{w(min)}$. Fracture toughness in terms of J_c may also serve as a fracture parameter with a two-parameter (α, β) Weibull distribution given by

$$P_f\left(J_c\right) = 1 - \exp\left[-\left(\frac{J_c}{\beta}\right)^\alpha\right] \tag{6}$$

A calibration scheme was proposed by Gao et al., [16] to determine unique values of the Weibull parameters (m, $\sigma_{w(u)}$) in Eq. (5) from fracture-toughness data measured under low- and high-constraint conditions. In an iterative process, the available toughness data at two levels of constraint are mapped back to a small-scale yielding (SSY) Weibull stress space where α in Eq. (6) takes on the theoretical value of 2 for Weibull distributions expressed in terms of J_c. Thus, the mapping to SSY space converts the problem to one that is solved through application of a one-parameter point-estimation procedure for determining β. The procedure seeks the m-value that results in the constraint-adjusted toughness distributions having the same statistical properties (α,β) in SSY space with α = 2. The converged m-value depends on the choice of equivalent tensile stress (i.e., HYDRO or MPS) used to define the Weibull stress [Eq. (4)], but the converged value of β will be unique in SSY space.

Application of the calibration procedure to the fracture-toughness data generated from Plate 14A material at a test temperature of –20 °C is depicted in Figs. 9 and 10. Calibration values of m = 2.64 (HYDRO) and m = 4.86 (MPS) were used in Eq. (4) to generate Weibull stress versus J-integral load paths from finite element solutions for shallow-flaw, deep-flaw, and SSY models (see Fig. 9). Results for the Weibull parameter based on the HYDRO stress are given in Fig. 9 (a) and on MPS in Fig. 9(b), respectively. These curves provided the basis for projecting fracture-toughness data back to SSY space along paths of constant Weibull stress. Given the constraint-adjusted toughness data, the scale parameter, β, was calculated from the maximum-likelihood point estimate (without small sample biasing) equation

$$\beta = \sqrt{\frac{1}{n}\sum_{i=1}^{n}\left(J_{(i)-SSY}\right)^2} \tag{7}$$

where $J_{(i)\text{-}SSY}$ are the toughness data for a given flaw-depth that were constraint-adjusted back to the SSY condition. In Fig. 10, iterations on the m-parameters were continued until convergence was achieved in β for m = 2.64 (HYDRO) and m = 4.86 (MPS). These two Weibull stress calibrations produced the unique scale parameter value of β = 86 kJ/m^2. Values for the remaining parameters in the right-hand side of Eq. (5), i.e., $\sigma_{w(u)}$ and $\sigma_{w(min)}$, are given for the calibrations based on the HYDRO and MPS parameters in Figs. 9(a) and (b), respectively. In Fig. 11, the predicted failure probability curves for the high- and low-constraint conditions [Figs. 11(a) and (b) for HYDRO, Figs 11(c) and (d) for MPS] are compared to the rank median estimates for the data calculated by the order statistic for the ith data point,

$$P_{f(i)} = \frac{i-0.3}{n+0.4}\ , \tag{8}$$

where n is the number of data points. More detailed descriptions of the Weibull calibration procedure are provided by Gao et al. [16] and Williams et al. [11].

4. Evaluation of Results

4.1 Applications of Master Curve Procedure

The test matrix was defined with the objective of generating K_{Jc} values for both shallow- and deep-flaw specimens that satisfy the specimen-size requirements given in ASTM E1921 [6]. The limiting K_{Jc} for specimens used in the testing program is given by

$$K_{Jc(\lim it)} = \left(\frac{Eb_o\sigma_{ys}}{M}\right)^{1/2} \tag{9}$$

where, E = material elastic modulus = 182,711 MPa at –20°C,

b_o = initial remaining ligament = 0.0254 m,

σ_{ys} = material yield stress = 652 MPa,

and, M = factor to establish specimen size requirements = 30.

Thus,

$$K_{Jc(\lim it)} = 317.6\, MPa\sqrt{m} \quad . \tag{10}$$

The value of b_o given above is for the deep-flaw specimen. When the limiting value [Eq. (10)] is compared with fracture-toughness data in Tables 1 and 2, it can be seen that all experimental values satisfy the ASTM limiting toughness for this size specimen. Thus, none of the data were censored according to the procedures of ASTM E1921 [6].

Applications of ASTM E1921 procedures to fifteen shallow-flaw tests (excluding PBS16) and seven deep-flaw tests performed at -20 °C produced T_o values of -69.1 °C and -42.3 °C, respectively. Thus, the shallow-flaw data produced a shift in reference temperature of ΔT_o = -26.8 °C relative to the deep-flaw specimens for this particular material and *a/W* ratio. If PBS16 is included in the shallow-flaw data, the resulting T_o is -68.2 °C with a shift of ΔT_o = -25.9 °C. Weibull plots of the shallow-flaw and deep-flaw data are shown in Figs. 12 and 13, respectively. A comparison of the two full data sets is shown in Fig. 14, which illustrates the shift in T_o toward lower temperatures with decreasing constraint.

As a check on the consistency and validity of the 1T deep-flaw data generated herein, these data are compared with a database of Plate 14A 1/2T C(T) results [9] in Fig. 15. The 1/2T C(T) data were size-adjusted to 1T, and then T_o was calculated using the Maximum Likelihood Estimator (MLE), excluding data points at -130 °C and 23 °C as being outside the range of T_o ± 50°C [6]. The value of T_o determined for the 1/2T C(T) data set is -48.2 °C as compared to -42.3 °C calculated for the seven deep-flaw specimens tested at -20 °C. Thus, the deep-flaw data appear to be consistent with the larger data set and fully representative of the Plate 14A material.

As was noted above, the shallow-flaw data set was well represented by the Master Curve Weibull model (see Fig. 12), even though the shallow-flaw value of T_o was significantly different from the deep-flaw value. A graphical comparison of the parent populations estimated by the two data sets is shown in Fig. 16, which shows the Weibull failure probability density function,

$$f\left(K_{Jc} \mid K_o\right) = \frac{4\left(K_{Jc} - 20\right)^3}{\left(K_o - 20\right)^4} \exp\left[-\left\{\frac{\left(K_{Jc} - 20\right)}{\left(K_o - 20\right)}\right\}^4\right] \tag{11}$$

for each data set with K_{Jc} and K_0 in MPa√m. In Eq. (11), the value of the scale parameter K_o was estimated by ASTM E1921 procedures where the location parameter is fixed at 20 MPa√m, and the shape parameter is fixed at 4. Figure 16 depicts two data sets with distinctly different estimated parent populations distinguised only by different scale parameters, K_o.

4.2 Constraint-Adjustment of Fracture-toughness Data

Data from the Plate 14A shallow-flaw 1T SE(B) specimens were constraint-adjusted to a deep-flaw (a/W = 0.5) 1T configuration using the Weibull parameters (m, $\sigma_{w(u)}$) determined in the previous section, and the procedure is illustrated graphically in Fig. 17. The fifteen constraint-adjusted shallow-flaw data were analyzed using the ASTM E1921 procedure [6] to obtain a value of T_o = -40.4 °C, which compares well with the value of -42.3 °C calculated for the deep-flaw specimens. The adjusted shallow-flaw data are shown in the Weibull plot of Fig. 18, along with the deep-flaw toughness data from Fig. 13. Failure probability density curves for the parent populations estimated by the constraint-adjusted shallow-flaw data and the deep-flaw data are shown in Fig. 19.

The ASTM E1921 procedure was applied to both shallow-flaw and deep-flaw Plate 14A 1T data following constraint-adjustment of the two data sets to SSY space [see Fig. 9(a) and (b)]. Those applications produced T_o values of –33.6 °C (shallow-flaw) and –34.2 °C (deep-flaw). Thus, the mapping to SSY space resulted in a transition temperature shift of ΔT_0 = -35.5 °C relative to the original shallow-flaw data. Figure 20 presents a Weibull plot of the deep-flaw and constraint-adjusted shallow-flaw (K_{Jc}, p_f) data compared to their corresponding Master Curve Weibull models.

Summaries of the Weibull parameters and T_o estimates for the constraint-adjusted data, the latter derived from HYDRO and MPS definitions of the Weibull stress, are given in Table 3. In Fig. 21, both unadjusted and adjusted fracture-toughness data are compared with Master Curve percentiles; scaling is based on the HYDRO and MPS parameters in Fig. 21(a) and (b), respectively. As expected, the definition of the equivalent stress had no influence on results obtained from applications of ASTM E-1921 to the Plate 14A data sets.

5. Conclusions

Testing of comparable shallow-flaw and deep-flaw 1T SE(B) specimens has further demonstrated the enhanced median toughness of shallow flaws over that of deep flaws. Evaluation of the original data showed the existence of a significant shift in T_o for shallow flaws as compared to deep flaws in the same size specimen. While insufficient data were generated to define the full shape of the shallow-flaw fracture-toughness curve, there is the potential for such a curve to have

a different shape than that of a deep-flaw curve. If so, this would require re-evaluation of some constants in the master curve equation.

From analyses of the constraint-adjusted shallow-flaw data, several specific conclusions and observations can be made.

(a) A transition shift of –26.8 °C was determined for shallow-flaw 1T SE(B) specimens with a/W = 0.10, compared to the deep-flaw 1T SE(B) specimen data.

(b) When both shallow-flaw and deep-flaw data sets were constraint-adjusted to SSY space, the calculated values of T_o were essentially identical. The transition temperature shift for shallow-flaw and deep-flaw data to SSY space was -35.5 °C and -8.1 °C, respectively.

References

1. T. H. Theiss and D. K. M. Shum, "*Experimental and Analytical Investigation of the Shallow-Flaw Effect in Reactor Pressure Vessels,*" USNRC Report NUREG/CR-5886 (ORNL/TM-12115), Oak Ridge National Laboratory, July 1992.

2. T. L. Dickson, W. J. McAfee, W. E. Pennell, and P. T. Williams, "Evaluation of Margins in the ASME Rules for Defining the P-T Curve for a RPV," pp. 47-72 in *Proceedings of the Twenty-Sixth Water Reactor Safety Meeting*, NUREG/CP-0166, Vol. 1, October 1998.

3. R. E. Link, Naval Surface Warfare Center, and J. A Joyce, U.S. Naval Academy, *"Application of Fracture Toughness Scaling Models to the Ductile-to-Brittle Transition,"* USNRC Report NUREG/CR-6279, January 1996.

4. W. E. Pennell, B. R. Bass, J. W. Bryson, Jr., T. L. Dickson and J. G. Merkle, *"Preliminary Assessment of the Effects of Biaxial Loading on Reactor Pressure Vessel Structural-Integrity-Assessment Technology,"* ORNL/NRC/LTR-94/31, Oak Ridge National Laboratory, August 1995.

5. T. L. Dickson, *"Review of the Pressurized-Thermal Shock Screening Criteria for Embrittled Pressurized Water Reactor Pressure Vessels"* ORNL/NRC/LTR-95/39, Oak Ridge National Laboratory, December 1995.

6. ASTM E 1921-97, *Standard Test Method for Determination of Reference Temperature, T_o, for Ferritic Steels in the Transition Range*, American Society for Testing and Materials, West Conshohocken, PA, ASTM Standard Vol. 03.01, Section 3, Metals Test Methods and Analytical Procedures, (1998) 1068-1084.

7. J. G. Merkle, K. Wallin, and D. E. McCabe, *"Technical Basis for an ASTM Standard on Determining the Reference Temperature, T_o, for Ferritic Steels in the Transition Range,"* USNRC Report NUREG/CR-5504 (ORNL/TM-13631), Oak Ridge National Laboratory, November 1998.

8. ASME Boiler and Pressure Vessel Code, Code Case N-629 (in process), *"Use of Fracture Toughness Test Data to Establish Reference Temperature for Pressure Retaining Materials of Section III, Division 1, Class 1,"* New York, 1998.

9. W. J. McAfee, B. R. Bass, P. T. Williams, and W. E. Pennell, *"The Effect of Specimen Size on Fracture Toughness Values Obtained From Large-Scale Cruciform Specimens Under Biaxial Loading,"* ORNL/NRC/LTR-99/12, Oak Ridge National Laboratory, June 1999.

10. B. R. Bass, W. J. McAfee, P. T. Williams, and W. E. Pennell, "Evaluation of Constraint Methodologies Applied to a Shallow-Flaw Cruciform Bend Specimen Tested under Biaxial Loading Conditions," *ASME/JSME Joint Pressure Vessels and Piping Conference*, San Diego, California, July 26-30, 1998.

11. P. T. Williams, B. R. Bass, and W. J. McAfee, "Application of the Weibull Methodology to a Shallow-Flaw Cruciform Bend Specimen Tested under Biaxial Loading Conditions," *31st National Symposium on Fatigue and Fracture Mechanics*, Volume STP 1389 (to be published), ASTM, Cleveland, OH, June 21-14, 1999.

12. C. Ruggieri, R. H. Dodds, Jr., and K. Wallin, "Constraint Effects on Reference Temperature, T_o, for Ferritic Steels in the Transition Region," *Engineering Fracture Mechanics* **60**(1), (1998) 19-36.

13. ASTM E 399-90, *Standard Test Method for Plane-Strain Fracture Toughness of Metallic Materials*, American Society for Testing and Materials, West Conshohocken, PA, ASTM Standard Vol. 03.01, Section 3, Metals Test Methods and Analytical Procedures, (1998) 413-443.

14. X. Gao and R. H. Dodds, Jr., "A Weibull Stress Model to Predict Cleavage Fracture in Plates Containing Surface Cracks," *Fatigue & Fracture of Engineering Materials and Structures* **22**, (1999) 481-493.

15. K. Wallin, *"Optimized Estimation of the Weibull Distribution Parameters,"* Research Report 604, Technical Research Center of Finland, Espoo, Finland, 1989.

16. X. Gao, C. Ruggieri, and R. H. Dodds, Jr., "Calibration of Weibull Stress Parameters using Fracture Toughness Data," *International Journal of Fracture* **92**, (1998) 175-200.

Table 1. Summary of Heat-treated Plate 14 Shallow-flaw SE(B) Data and Toughness Values Constraint-Adjusted to a Deep-Flaw Configuration.

Specimen Number	Test Temperature (°C)	Failure Load (kN)	$K_{Jc(\text{shallow-flaw})}$ (MPa√m)	$K_{Jc(\text{deep-flaw})}$ adjusted (MPa√m)
PBS1	-65	78.69	48.7	48.4[1]
PBS2	-55	328.06	153.4	122.8[1]
PBS3	-55	139.01	89.5	82.3[1]
PBS4	-55	109.83	69.5	66.4[1]
PBS5	-55	193.23	149.3	120.6[1]
PBS6	-20	223.52	258.5	157.5
PBS7	-20	190.83	161.2	123.7
PBS8	-20	198.21	167.0	126.5
PBS9	-20	186.25	155.0	120.7
PBS10	-20	226.86	274.0	160.8
PBS11	-20	207.11	193.6	137.8
PBS12	-20	170.41	120.5	101.5
PBS13	-20	210.76	224.2	148.3
PBS14	-20	172.64	128.4	106.3
PBS15	-20	228.51	283.1	162.5
PBS16	-20	103.42	63.6	61.5
PBS17	-20	217.70	219.6	146.9
PBS18	-20	229.08	270.0	160.0
PBS19	-20	208.53	205.6	142.2
PBS20	-20	211.29	213.8	145.0
PBS21	-20	214.36	233.0	151.0

[1]Approximate – adjusted using analysis based on –20 °C material properties.

Table 2. Summary of Heat-treated Plate 14 Deep-Flaw SE(B) Data.

Specimen Number	Test Temperature (°C)	Failure Load (kN)	K_{Jc} (MPa√m)
PBD1	-65	38.92	73.9
PBD2	-65	54.27	126.8
PBD3	-20	58.27	135.1
PBD4	-20	53.82	108.9
PBD5	-20	69.39	177.1
PBD6	-20	61.39	141.7
PBD7	-20	68.95	174.4
PBD8	-20	41.37	84.8
PBD9	-20	58.72	132.1

Table 3. Summary of Weibull Parameter and T_0 Estimates

(a) HYDRO Criterion

Case No.	Specimen Series	Flaw Depth *a/W*	Replicate Tests *N*	Constraint Condition *a/W* or SSY	Scale, K_0 (MPa√m)	Median (MPa√m)	T_0 (°C)
1	PBD	0.5	7	0.5	148.24	137.01	-42.34
2	PBD	0.5	7	SSY	131.47	121.71	-34.22
3	PBS	0.1	15*	0.1	225.93	207.90	-69.09
4	PBS	0.1	15*	0.5	144.04	133.18	-40.42
5	PBS	0.1	15*	SSY	130.34	120.68	-33.62

(b) MPS Criterion

Case No.	Specimen Series	Flaw Depth *a/W*	Replicate Tests *N*	Constraint Condition *a/W* or SSY	Scale, K_0 (MPa√m)	Median (MPa√m)	T_0 (°C)
1	PBD	0.5	7	0.5	148.24	137.01	-42.34
2	PBD	0.5	7	SSY	131.19	121.46	-34.07
3	PBS	0.1	15*	0.1	225.93	207.90	-69.09
4	PBS	0.1	15*	0.5	144.55	133.64	-40.65
5	PBS	0.1	15*	SSY	130.08	120.44	-33.48

*PBS16 was excluded from the data set.

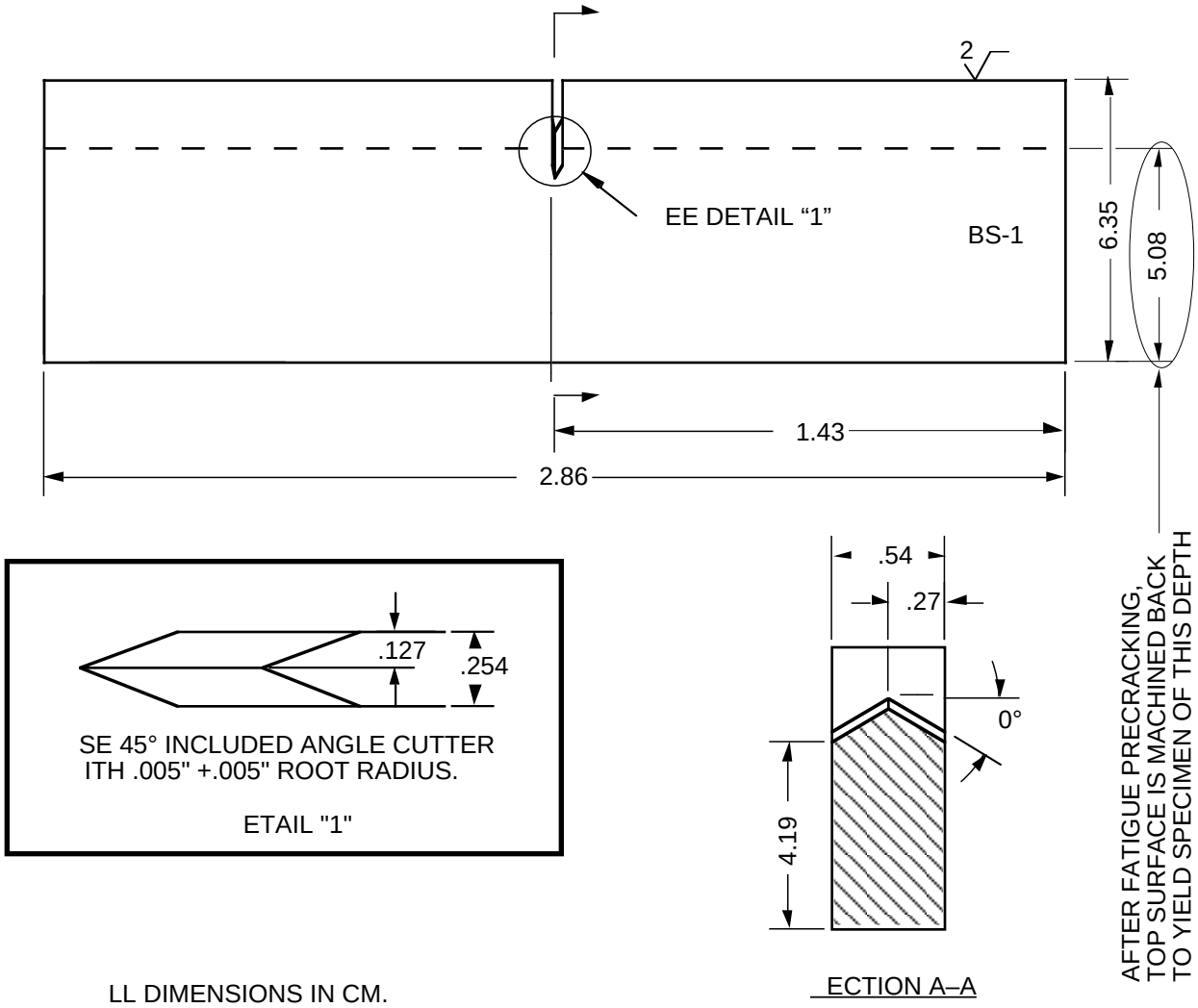

Fig. 1. Modified SE(B) specimen geometry to be used in fatigue precracking phase of shallow-flaw fracture specimens.

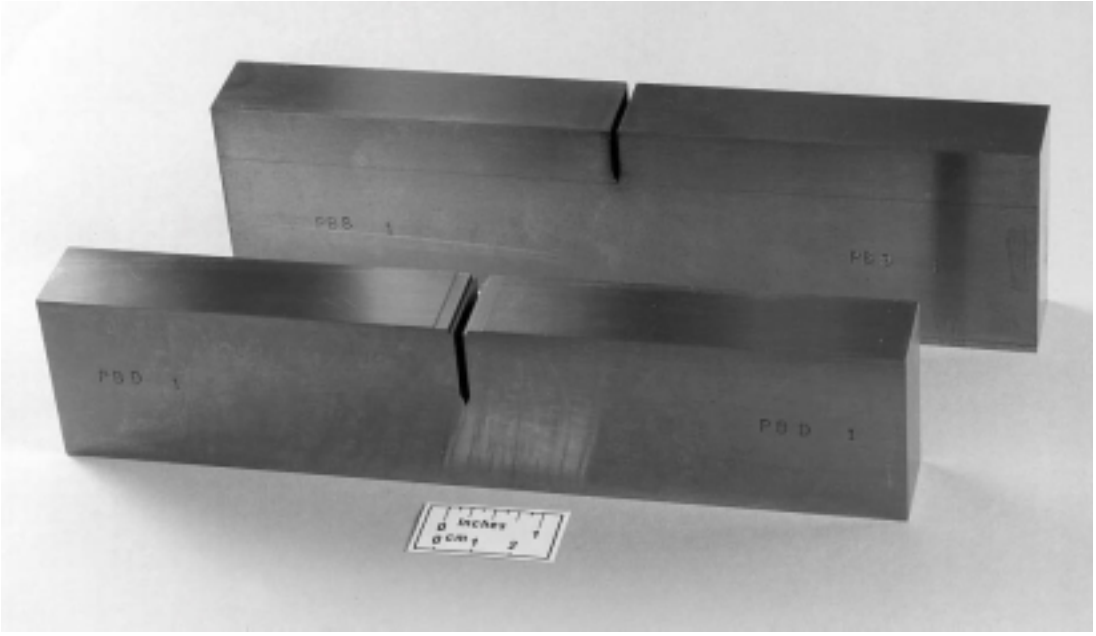

Fig. 2. Comparison of geometry of shallow-flaw (back) and deep-flaw (front) SE(B) specimens used in shallow-flaw effects on T_o study.

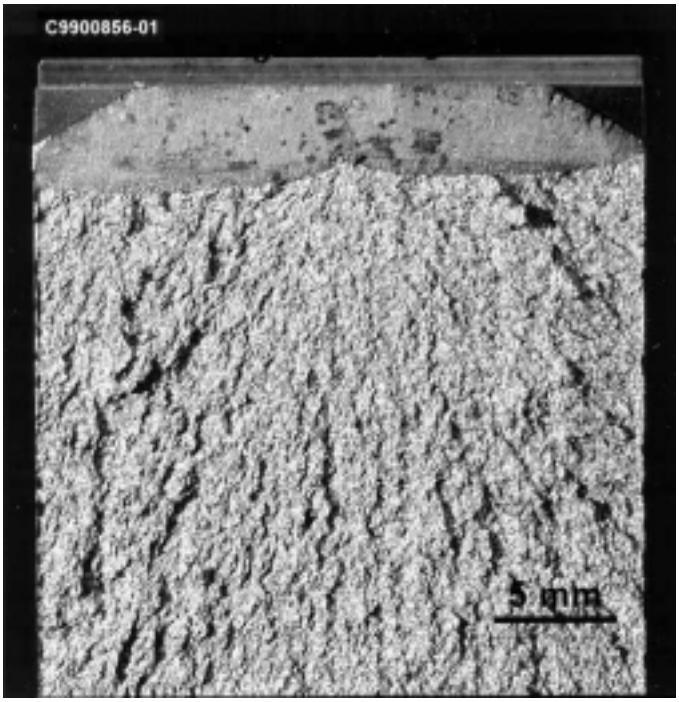

Fig. 3. Fracture surface for shallow-flaw SE(B) specimen PBS16 showing unique cleavage initiation site associated with apparent material defect.

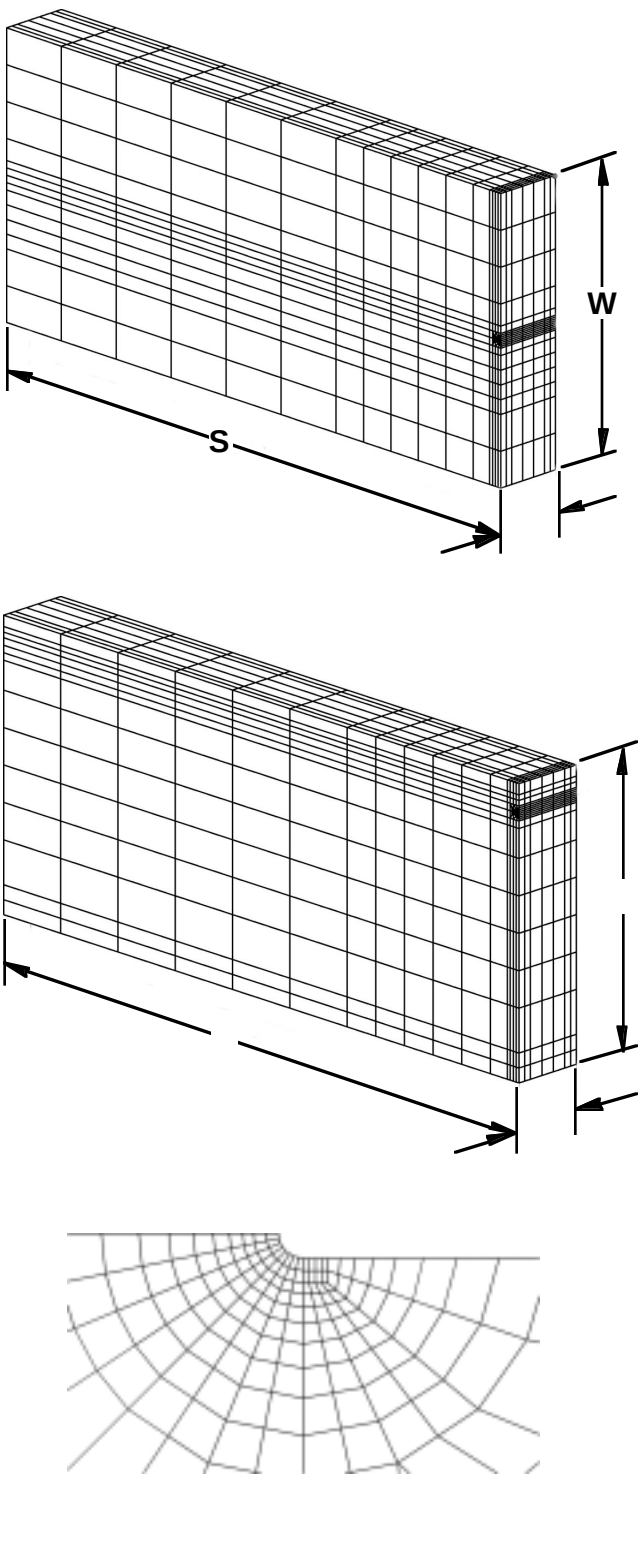

Fig. 4. Finite-element 1/4 models of bendbar specimens: (a) deep-flaw specimen, a/W = 0.5, (b) shallow-flaw specimen, a/W = 0.1 (S/W = 101.6 mm and W/B = 50.8 mm for both), and (c) close up of finite-root tip meshing for blunt-tip models.

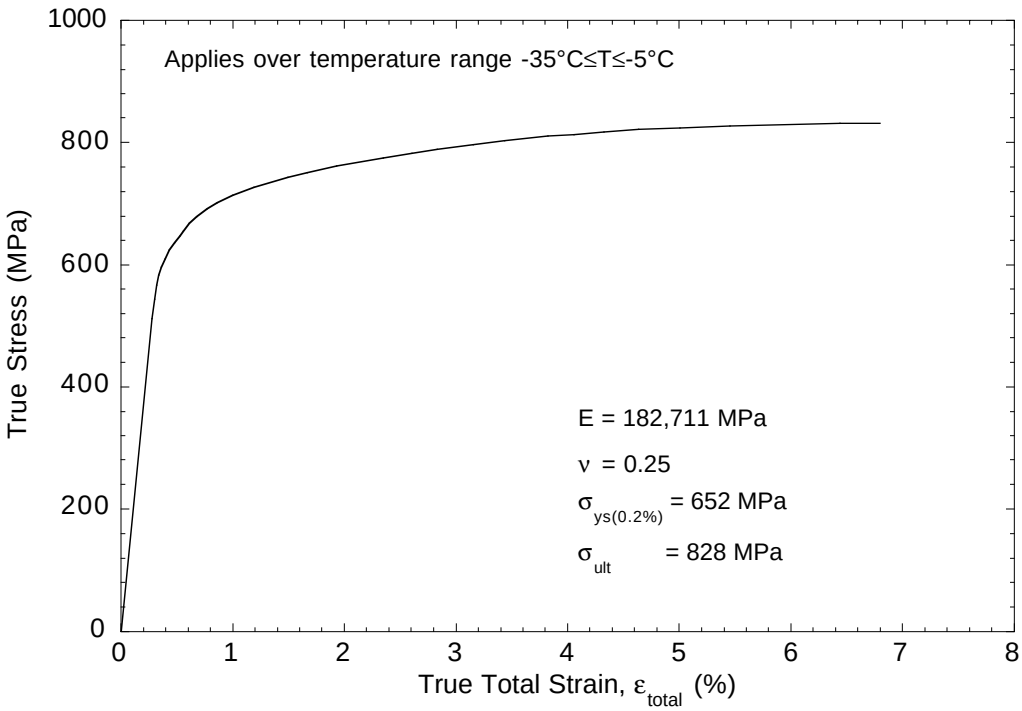

Fig. 5. True-stress vs true-strain curve used in analyses of Plate 14A bendbar specimens. Curve is taken from characterization data.

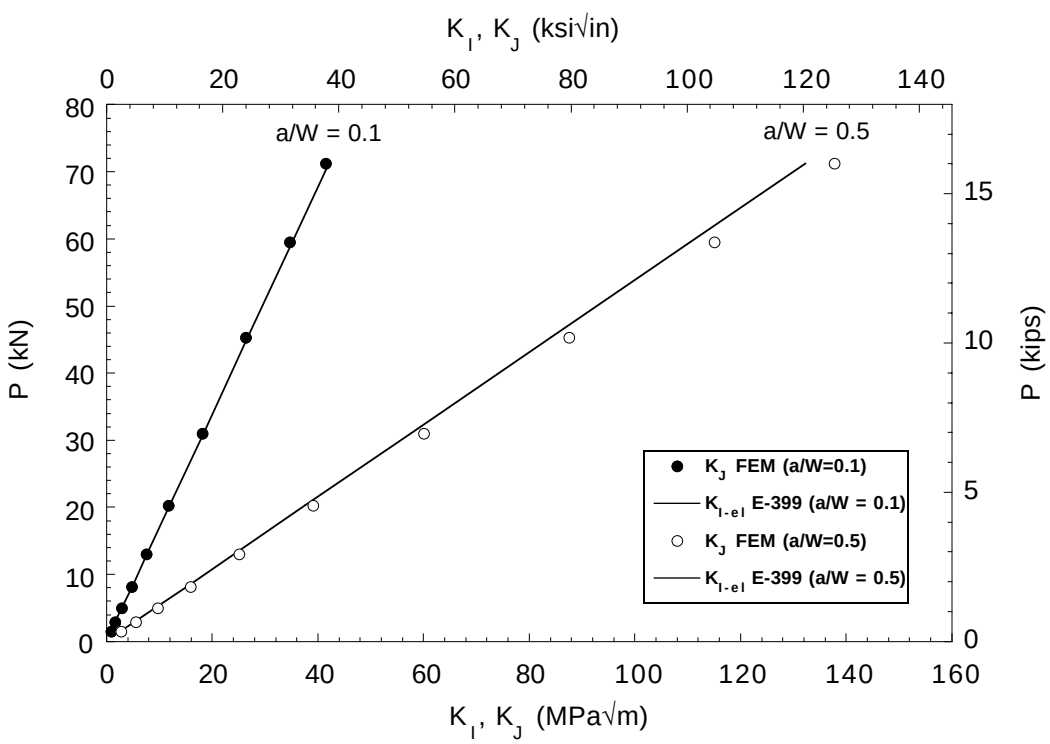

Fig. 6. Verification calculations for shallow-flaw and deep-flaw models: linear-elastic K_J compared to ASTM E-399 $K_{I\text{-}el}$.

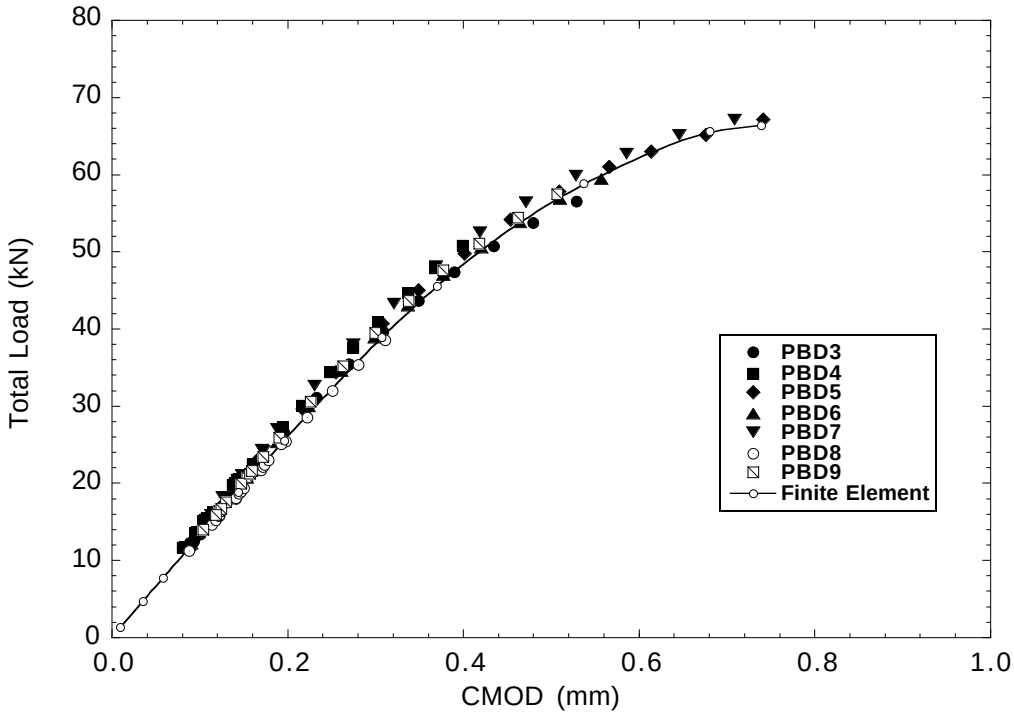

Fig. 7. Comparison of deep-flaw (*a/W* = 0.5) bendbar Load-CMOD experimental results with prediction from finite element analysis. All tests at -20 °C.

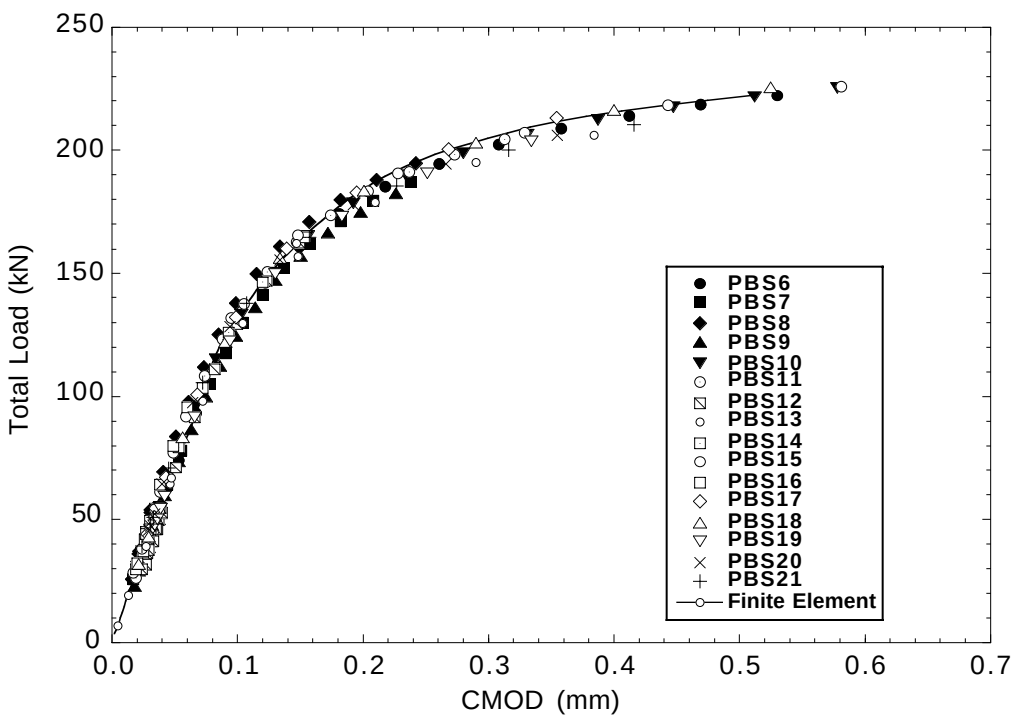

Fig. 8. Comparison of shallow-flaw (*a/W* = 0.1) bendbar Load-CMOD experimental results with prediction from finite element analysis. All tests at –20°C.

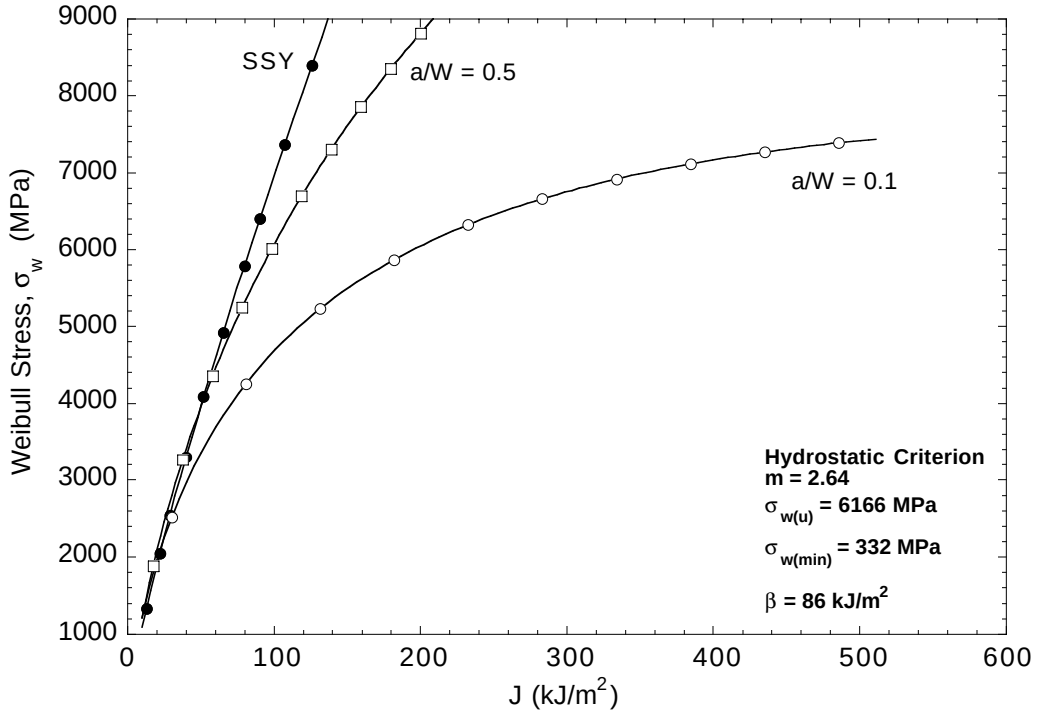

(a)

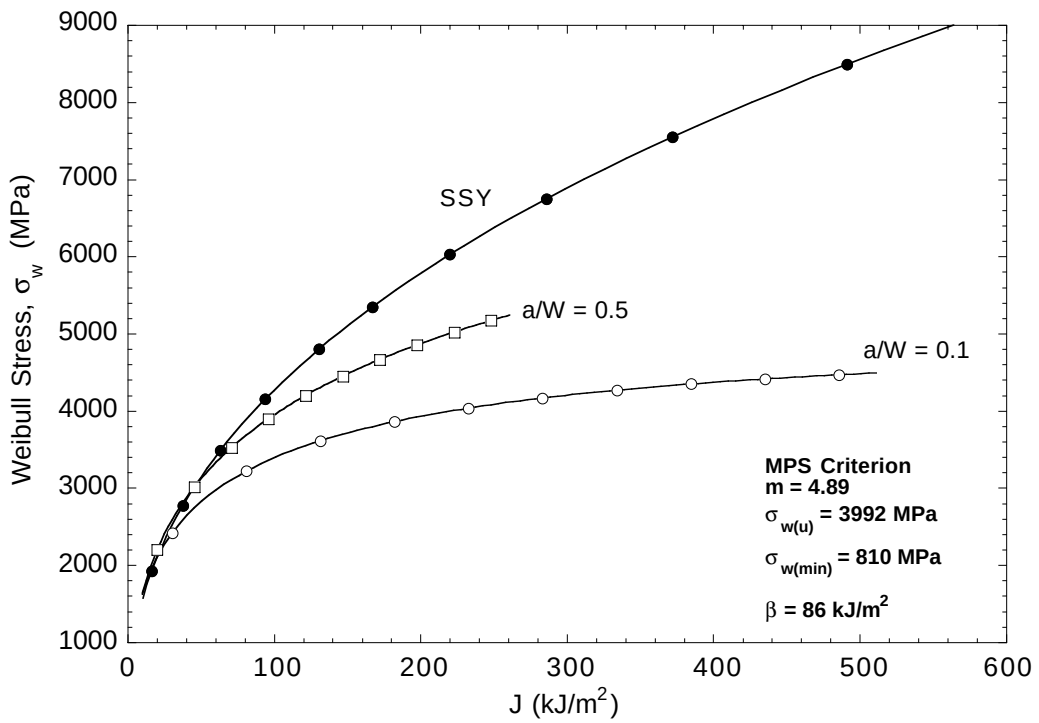

(b)

Fig. 9. Weibull stress trajectories for converged solutions of (a) hydrostatic stress and (b) maximum principal stress criteria.

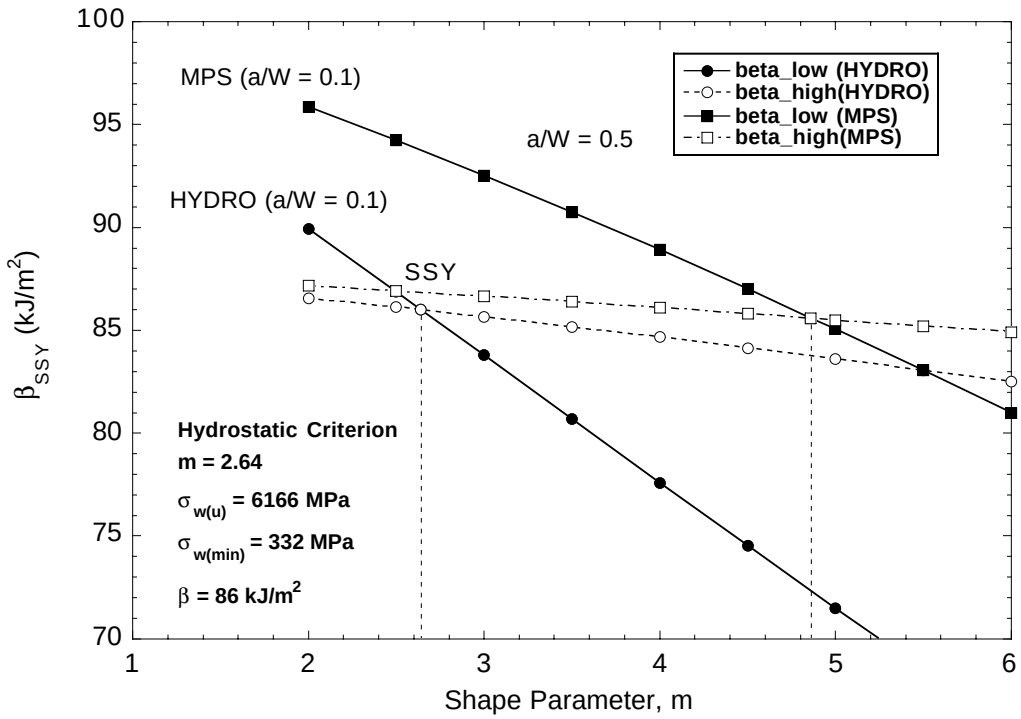

Fig. 10. Comparison of calibration results for maximum principal and hydrostatic stress fracture criteria**.**

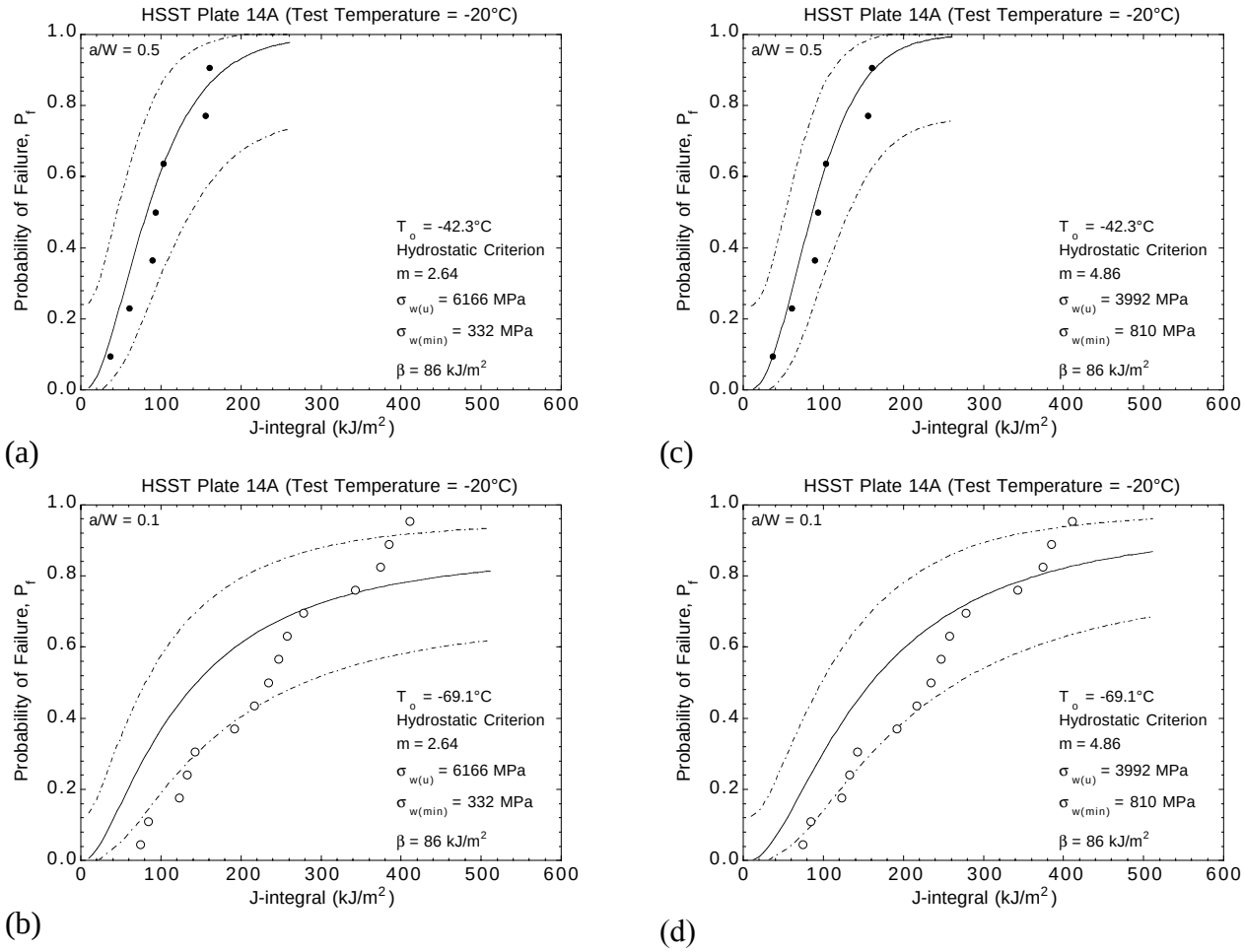

Fig. 11. Comparison of median rank failure probability estimates to model predictions for (a) high-constraint (*a/W*=0.5) HYDRO, (b) low-constraint (*a/W*=0.1) HYDRO, (c) high-constraint (*a/W*=0.5) MPS, and (d) low-constraint (*a/W*=0.1) MPS models. Dashed curves are 5 percent and 95 percent confidence bounds on median rank failure probability estimates.

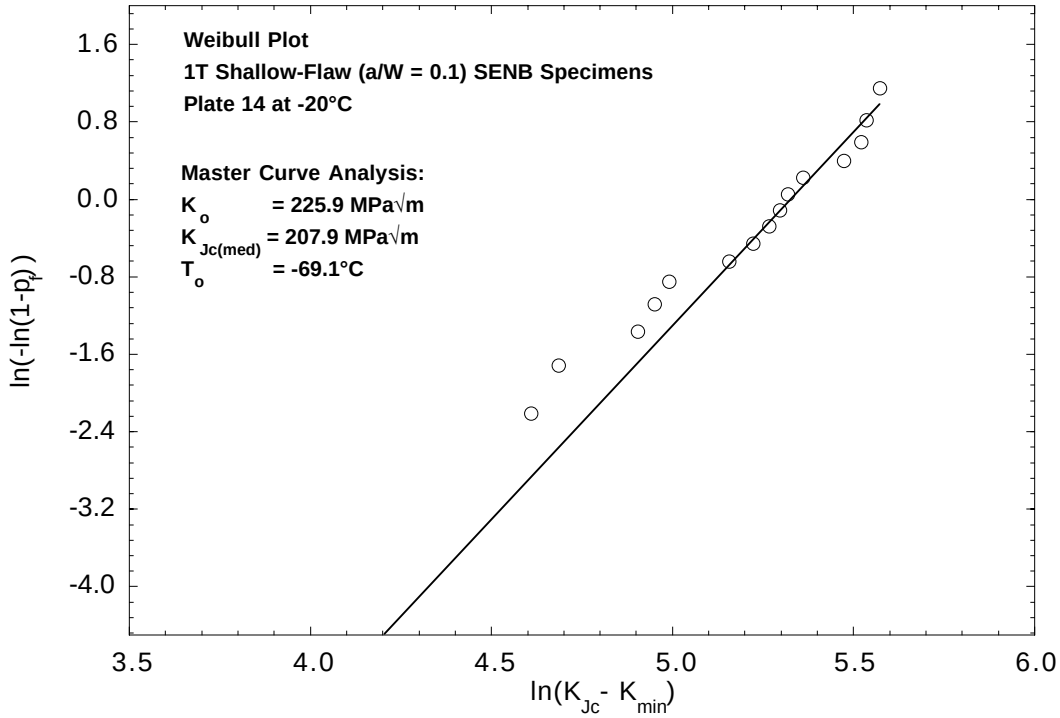

Fig. 12. Weibull plot of fifteen shallow-flaw K_{Jc} data points and their median rank failure probability estimates (p_f) compared to the Master Curve model.

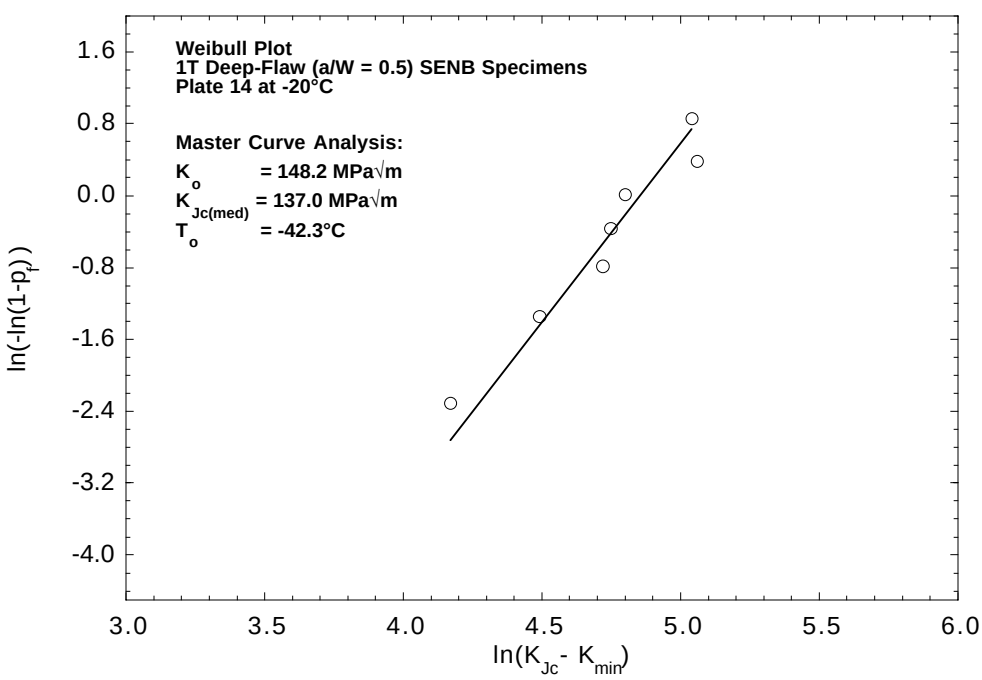

Fig. 13. Weibull plot of seven deep-flaw K_{Jc} points and their median rank failure probability estimates (p_f) compared to the Master Curve model

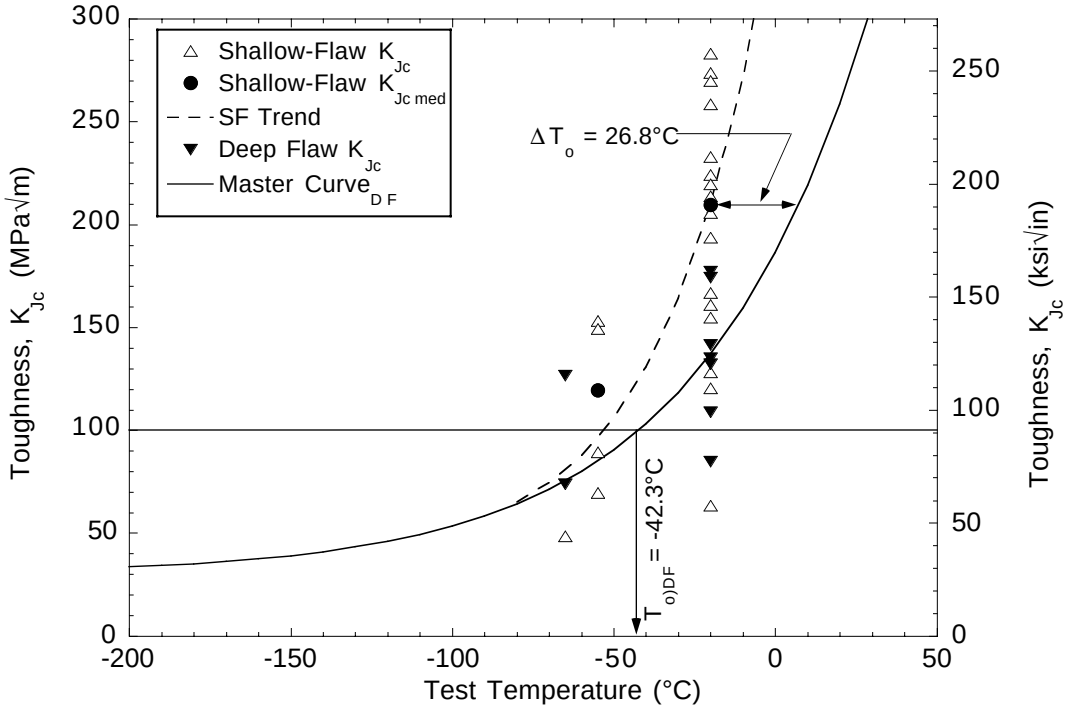

Fig. 14. Comparison of shallow-flaw and deep-flaw K_{Jc} results showing temperature shift of median of shallow-flaw set at -20 °C.

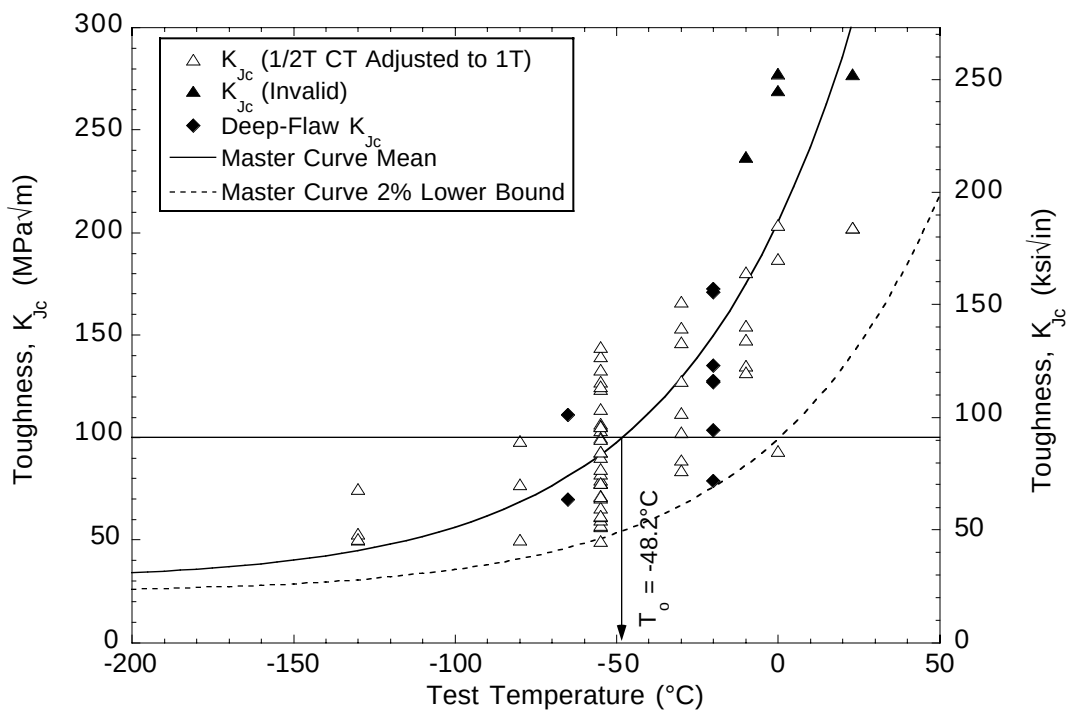

Fig. 15. Comparison of deep-flaw 1T SE(B) K_{Jc} results with database of 1/2T C(T) specimens size-adjusted to a 1T condition.

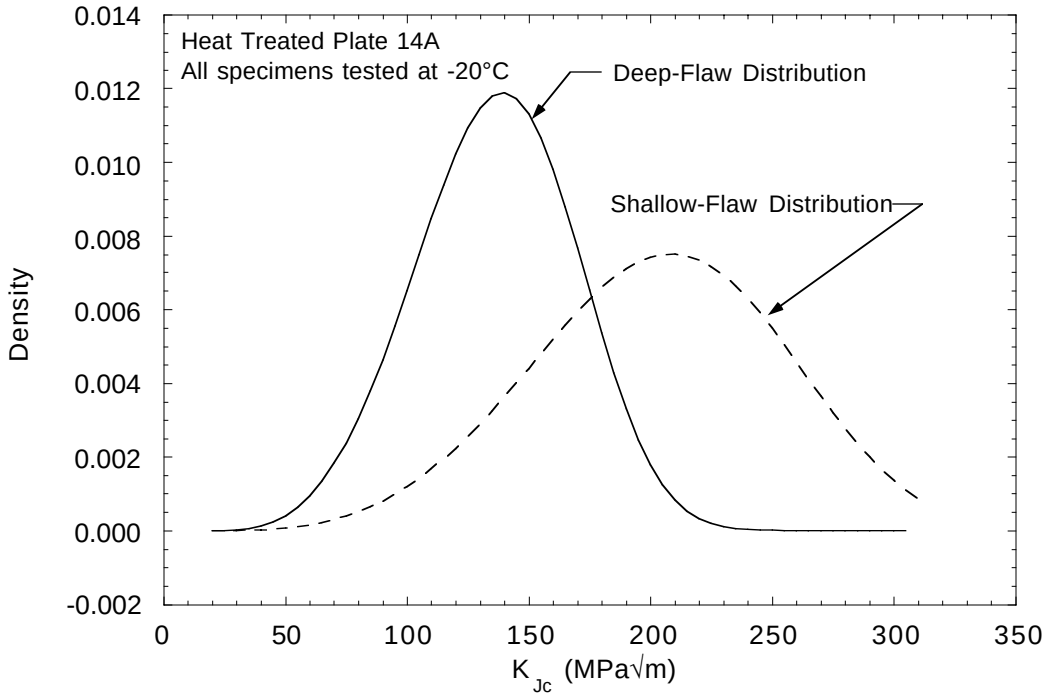

Fig. 16. Comparison of parent population Weibull probability densities estimated using deep-flaw and unadjusted shallow-flaw K_{Jc} data from 1T SE(B) specimens. Variation in densities is due to different maximum-likelihood (ML) point estimates for the shape parameter K_0.

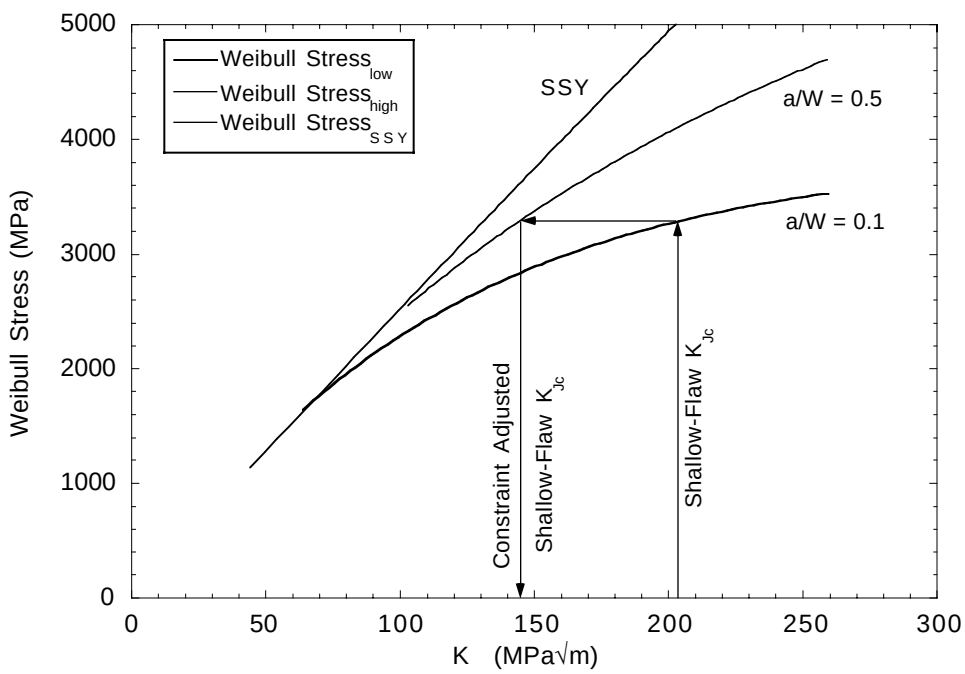

Fig. 17. Shallow-flaw K_{Jc} results were adjusted to deep-flaw constraint values using a numerical mapping along lines of constant Weibull stress from the a/W = 0.1 to the a/W = 0.5 load path.

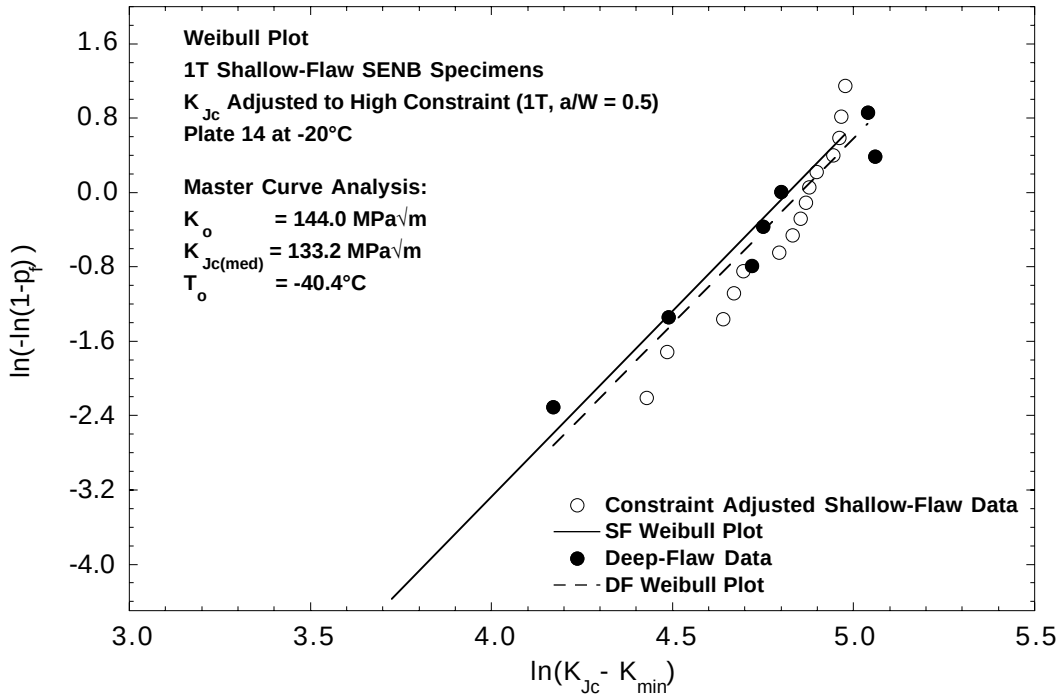

Fig. 18. Plot of seven deep- and fifteen shallow-flaw (K_{Jc}, p_f) data points with the shallow-flaw toughness values constraint-adjusted to a deep-flaw condition. The solid and dashed lines are the corresponding Master Curve Weibull models.

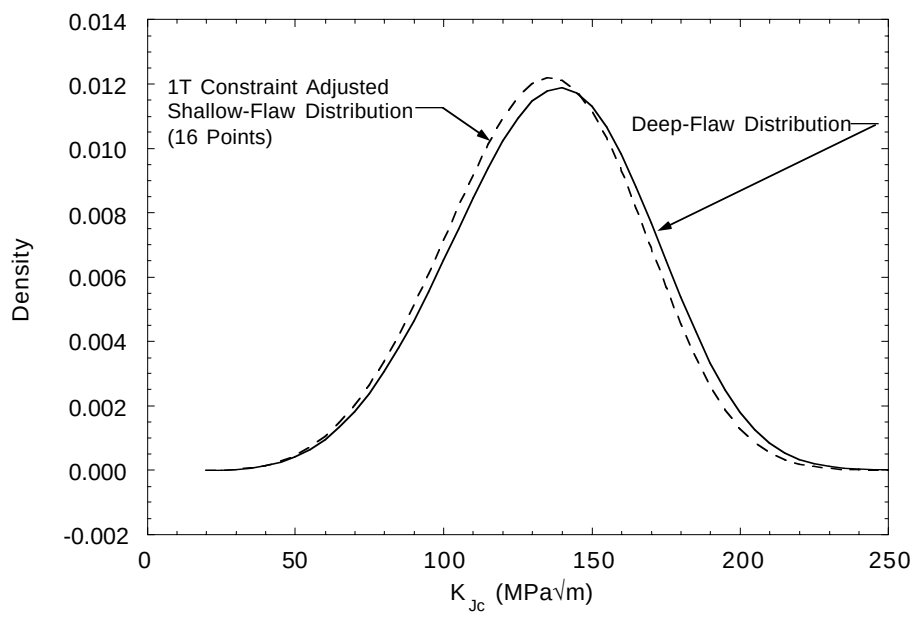

Fig. 19. Comparison of parent population Weibull probability densities estimated using deep- and shallow-flaw (constraint-adjusted to the deep-flaw condition) K_{Jc} results from 1T SE(B) specimens (heat-treated Plate 14, tests at –20 °C). Densities are based on the Master Curve Weibull model.

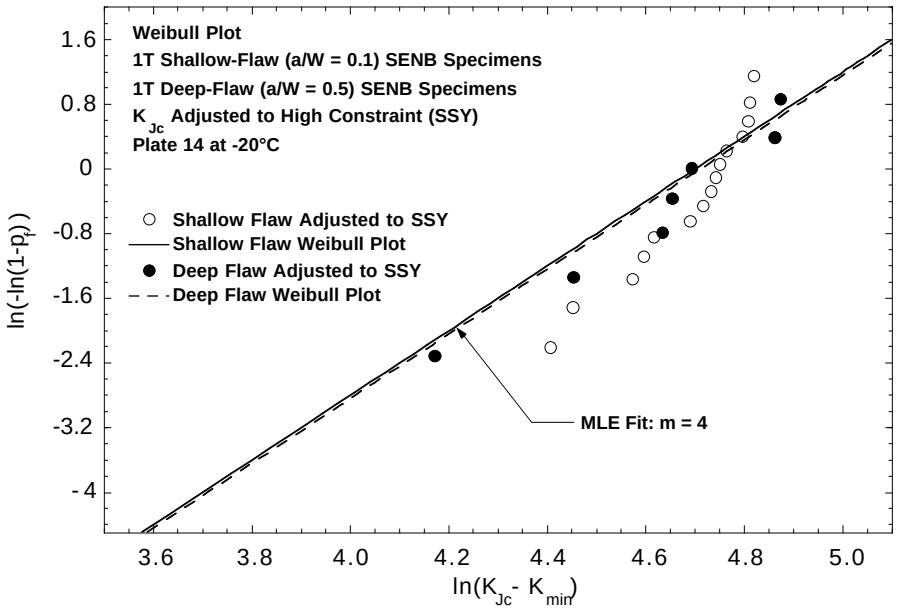

Fig. 20. Deep- (7 points) and shallow-flaw (15 points) (K_{Jc}, p_f) results constraint-adjusted to SSY, tests at -20 °C. Solid and dashed lines are the corresponding Master Curve Weibull models.

(a)

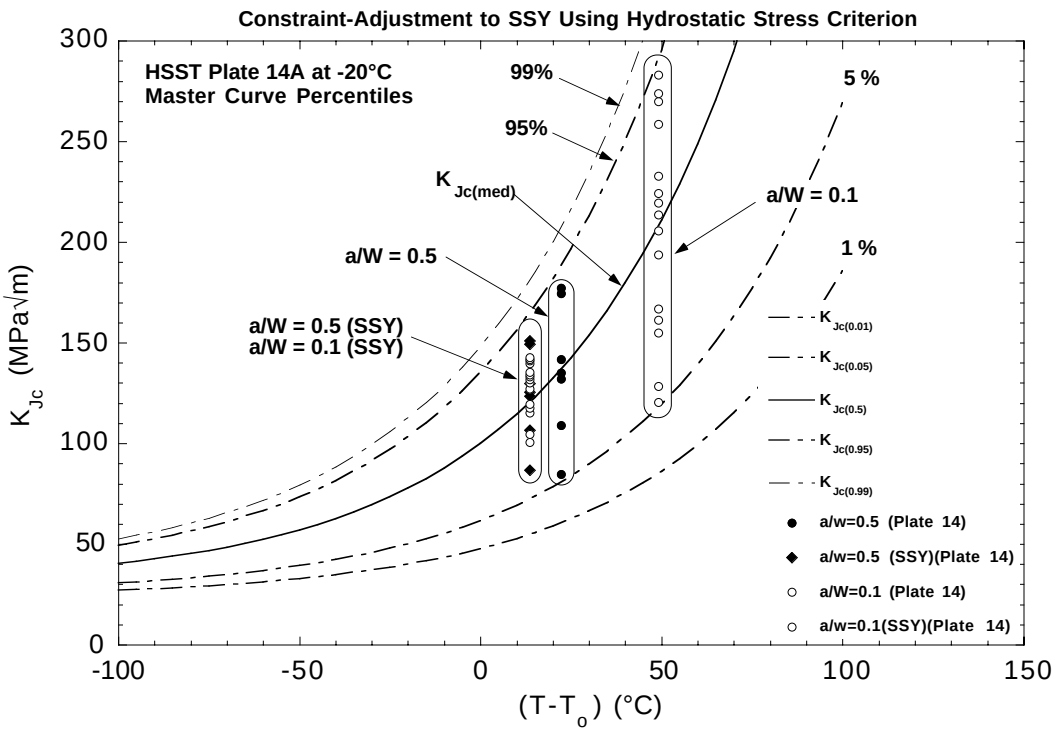

(b)

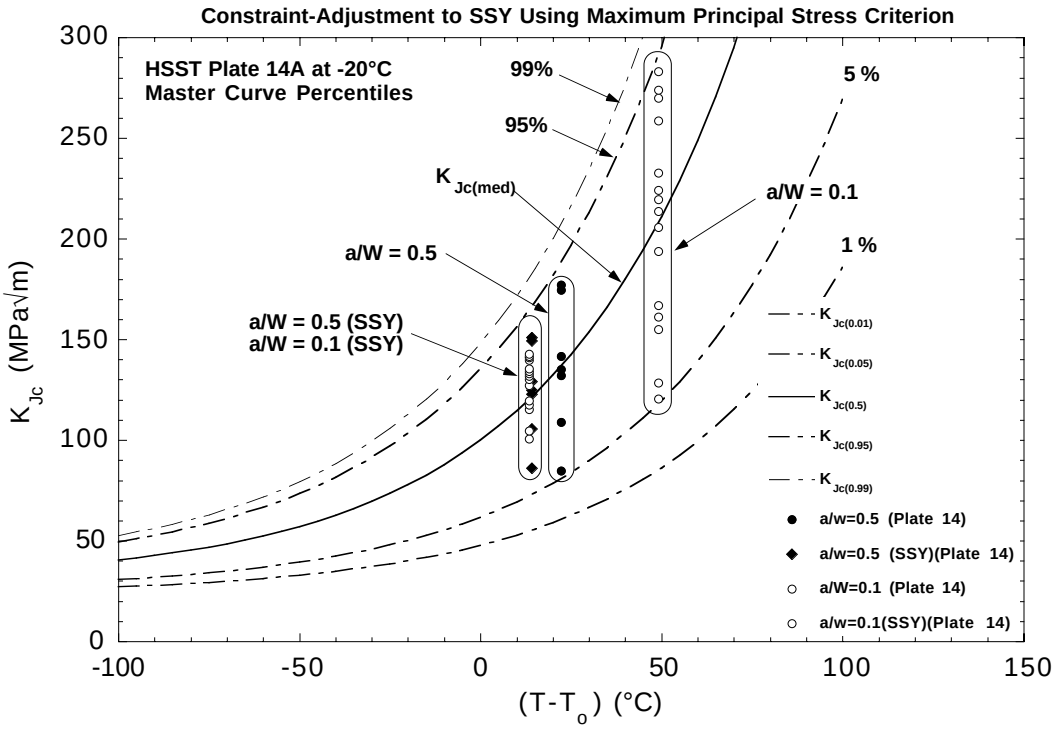

Fig. 21. Comparison of constraint scaling with resulting shift in T_0 for (a) hydrostatic stress and (b) maximum principal stress criteria. Solid and dashed lines are Master Curve Weibull model percentile curves.

Internal Distribution

1-5. B. R. Bass
6. W. G. Craddick
7. T. L. Dickson
8. D. M. Hetrick
9. M. A. Kuliasha
10. S. K. Iskander
11. W. J. McAfee
12. R. K. Nanstad
13-14. C. E. Pugh
15. T. M. Rosseel
16. J. J. Simpson
17. M. A. Sokolov
18-22. P. T. Williams
23. Laboratory Records

External Distribution

24. W. H. Bateman, NRR, U.S. Nuclear Regulatory Commission, MS O7 D4, Washington, D.C. 20555-0001
25. R. H. Dodds, 3140 Newmark Laboratory, 205 North Matthews, Urbana, IL 61801
26. C. J. Fairbanks, RES/DET/MEB, U.S. Nuclear Regulatory Commission, MS T-10 E10, Washington, D.C. 20555-0001
27. E. M. Hackett, RES/DET/MEB, U.S. Nuclear Regulatory Commission, MS T-10 E10, Washington, D.C. 20555-0001
28. J. A. Joyce, U.S. Naval Academy, Mechanical Engineering Department, MS 11C, 590 Hollway Road, Annapolis, MD 21402
29-33. M. T. Kirk, RES/DET/MEB, U.S. Nuclear Regulatory Commission, MS T-10 E10, Washington, D.C. 20555-0001
34-35. S. N. Malik, RES/DET/MEB, U.S. Nuclear Regulatory Commission, MS T-10 E10, Washington, D.C. 20555-0001
36. M. E. Mayfield, RES/DET, U.S. Nuclear Regulatory Commission, MS T-10 E10, Washington, D.C. 20555-0001
37. M. A. Mitchell, NRR, U.S. Nuclear Regulatory Commission, MS O7 D4, Washington, D.C. 20555-0001
38. C. G. Santos, RES/DET/MEB, U.S. Nuclear Regulatory Commission, MS T-10 E10, Washington, D.C. 20555-0001
39. W. J. Shack, Energy Technology Division, Argonne National Laboratory, 9700 S. Cass Avenue, Argonne, IL 60439
40. R. L. Tregoning, Fatigue and Fracture Branch, Carderock Division, Naval Surface Warfare Center, 9500 McArthur Blvd., West Bethesda, MD 20817-5700
41. K. R. Wichman, NRR, U.S. Nuclear Regulatory Commission, MS O7 D4, Washington, D.C. 20555-0001